

## Article

# Characterization of Propane Fueled Flames: A Significant Source of Brown Carbon

Jai Prakash <sup>1</sup>, Kalyan Mitra <sup>2</sup>, Harsh Raj Mishra <sup>3</sup>, Xiangyu Pei <sup>2,†</sup>, Evert Ljungström <sup>2</sup>  
and Ravi Kant Pathak <sup>2,3,\*</sup>

<sup>1</sup> Department of Atmospheric Science, School of Earth Sciences, Central University of Rajasthan, Bandarsindri, Kishangarh, Ajmer 305817, India

<sup>2</sup> Atmospheric Science, Department of Chemistry and Molecular Biology, University of Gothenburg, 41296 Gothenburg, Sweden

<sup>3</sup> Indo Gangetic Plains—Center for Air Research and Education (IGP-CARE), RuriPara, Hamirpur 210501, India

\* Correspondence: ravikant@chem.gu.se

† Current Affiliation: College of Environmental and Resource Sciences, Zhejiang University, Hangzhou 310058, China.

**Abstract:** In this study, we developed a framework for interpreting the in situ morphological properties of black carbon (BC, also referred to as “soot” due to combustion relevance) mixed with primary organic aerosol. Integration of the experiment considering primary organic aerosol (POA) evaporation from the soot particles was examined using a Differential mass–mobility analyzer (DMA) and showed the untold story of the mixing of BC and POA. We also hypothesize that morphological transformation of soots and determined such as (i) the evaporation of externally and internally mixed POA led to a decline in the particle number and size of monodisperse aerosol; (ii) presence of externally mixed BC was interpreted from the occurrence of two peaks of soot upon heating; (iii) heat-induced collapse of the BC core possibly resulted from the evaporation of material from the voids and effect of heat; (iv) volume equivalent to changes in the mobility diameter represented evaporation of POA from the surface and collapse upon heating. POA constituted a high fraction (20–40% by mass) of aerosol mass from these flames and was predominantly (i.e., 92–97% by mass) internally mixed with BC. POA was found to be highly light absorptive, i.e., an Ångström absorption exponent (AAE) value of (in general)  $>1.5$  was estimated for BC + POA at 405/781 nm wavelengths. Interestingly, a much more highly absorptive POA [mass absorption cross-section (MAC)- $5 \text{ m}^2 \text{ g}^{-1}$ ] at 405 nm was discovered under a specific flame setting, which was comparable to MACs of BC particles ( $8\text{--}9 \text{ m}^2 \text{ g}^{-1}$ ).

**Keywords:** flame burner; BrC; POA; morphology; optical characteristics



**Citation:** Prakash, J.; Mitra, K.; Mishra, H.R.; Pei, X.; Ljungström, E.; Pathak, R.K. Characterization of Propane Fueled Flames: A Significant Source of Brown Carbon. *Atmosphere* **2022**, *13*, 1270. <https://doi.org/10.3390/atmos13081270>

Academic Editor: Patricia K. Quinn

Received: 11 July 2022

Accepted: 6 August 2022

Published: 10 August 2022

**Publisher's Note:** MDPI stays neutral with regard to jurisdictional claims in published maps and institutional affiliations.



**Copyright:** © 2022 by the authors. Licensee MDPI, Basel, Switzerland. This article is an open access article distributed under the terms and conditions of the Creative Commons Attribution (CC BY) license (<https://creativecommons.org/licenses/by/4.0/>).

## 1. Introduction

Aerosol particles play a significant role in the atmospheric processes of the planet [1–3]. Particles, either directly emitted or formed through secondary processes, can reflect sunlight, and serve as cloud condensation nuclei (CCN) in cloud-forming processes. Both processes result in the cooling of the Earth's surface. However, black carbon (BC) or soot differs from other types of particles, owing to its strong sunlight-absorption ability, which leads to the warming of the planet. BC is the second most important human-emitted pollutant from the viewpoint of the warming effect; only carbon dioxide has a larger effect [1]. This material is co-produced with other primary gas and aerosol components due to the incomplete combustion of fuel. Owing to atmospheric transformations that lead to changes in its properties, BC is an elusive particulate matter, despite being a primary pollutant from combustion processes. These transformations are induced by its interaction with other gas and aerosol components, such as organic aerosol (OA) [4]. The other key component formed in the combustion process, i.e., primary organic aerosol (POA), can also contribute to light absorption (especially in the

ultra-violet (UV) to visible light wavelength range). POA leading to absorption in this range is collectively referred to as brown carbon (BrC) [5–7]. Determining the in situ hygroscopic and optical properties of soot is especially challenging, owing to the mixing and morphological states of soot-containing BC and POA mixture.

Previous studies have outlined several techniques, including single-particle techniques and population-averaged techniques, for determining the mixing state of BC-containing particles. The single particle techniques include scanning electron microscopy (SEM) [8], refractory BC (rBC) incandescence, e.g., the single particle soot photometer (SP2) [9], and particle mass spectrometry, e.g., light scattering soot particle aerosol mass spectrometer (LS-SP-AMS) [10,11]. The tandem differential mobility analyzer (TDMA) technique is a commonly used particle population averaged technique. With this technique, a certain mobility diameter of the aerosol is selected with the first DMA. The condensed material is then removed or added by modifying (through denuding or coating) the monodisperse aerosol. This modification is followed by the second DMA, where changes in the mobility diameter are tracked. In order to quantify the particle mass before and after the denuding/coating process, a particle mass analyzer (e.g., aerosol particle mass analyzer (APM) or centrifugal particle mass analyzer (CPMA)) can be used either after or to replace the second DMA. In addition, the mass–mobility relationship, which determines the particle morphology, can be derived by using a DMA-APM/CPMA setup. This technique has been used to characterize the volatile and non-volatile mass fraction of BC-POA mixture particles resulting from the combustion of propane in a shock tube [12], flames of burners [13], a natural gas-direct-injection compression-ignition engine [14], gasoline direct injection engines [15], and a diesel engine [16].

The optical properties of BC may be changed through mixing with organic aerosol. In the atmosphere, an organic aerosol is a mixture of thousands of organic compounds consisting of secondary organic aerosol (SOA) that is typically considered non-light absorbing. However, recent results have suggested that organic aerosol contains BrC. The emissions of POA with BrC components have been associated with different sources, such as biomass burning [17–19], fossil fuel combustion [20,21], smoldering combustion [22], and natural biogenic emissions [23]. The formation of BrC has also been attributed to aging and heterogeneous reactions of secondary organic aerosol (SOA) [24]. The absorption wavelength dependence of light-absorbing aerosols is commonly described by the Ångström absorption exponent (AAE). The complex refractive index (RI),  $m = n - ik$ , is the fundamental parameter determining the optical properties of particles, where the real part ( $n$ ) and the imaginary part ( $k$ ) represent scattering and absorption, respectively. BC is the most efficient light-absorbing aerosol in the atmosphere, with a mass absorption cross-section (MAC) of  $\sim 7.5 \text{ m}^2 \text{ g}^{-1}$  at a wavelength of 550 nm [4]. The AAE for BC is typically considered as being  $\sim 1$  [5,25], and a wavelength-independent RI, i.e., 1.95–0.79i, is commonly assumed [4]. However, the MAC of BrC exhibits a considerably stronger wavelength dependence than the MAC of BC (AAE range of 2–6) [6,26] due to the strong wavelength-dependent imaginary part of RI [27]. BrC may account for 20–50% of particle light absorption in the UV wavelength range [28–30] and thereby influence the radiative balance and photochemistry in the troposphere. Nevertheless, the light-absorption properties of BrC are poorly represented in the conventional climate and chemical transport models as most models still treat OA as non-absorbing (i.e.,  $k_{\text{OA}} = 0$ ). Hence, the overall warming effect of carbonaceous aerosols remains ambiguous and uncertain. Models providing a better representation and description of BrC formation and properties than that provided by the current models are therefore desirable. However, an improved understanding of the formation mechanism, morphological state as well as hygroscopic and optical properties of the co-produced BC and POA mixture from the combustion processes are required for developing these models. This is especially true for the link between combustion-generated POA and its light-absorption potential. A detailed systematic characterization of size-resolved BC and POA freshly co-emitted from various combustion systems is essential for elucidating the gross atmospheric impact and warming potential of these substances.

In this study, the morphology and optical characteristics of combustion aerosol particles containing BC and POA from a new custom-built premixed-cum-diffusion flame burner were systematically investigated. A framework for interpreting the mixing and morphological state of soot containing BC and a POA mixture is developed. The in situ morphological states of soot from three different flames were derived. In addition, the fractions of light absorbing POA (i.e., BrC) mixed with BC and its interlinked MACs were quantified for size-resolved soot particles. The parameterization linking MAC and RI of BrC is also developed. These parameters can be embedded in climate and chemical transport models. More importantly, these results facilitate an improved understanding of soot morphology as well as the properties and formation of BrC in combustion processes. These results also provide insights into the design of experimental matrices for (i) the characterization of emissions from other combustion systems and (ii) BC transformation and aging studies.

## 2. Experimental

### 2.1. Design of Burner

In order to perform controlled experiments in the laboratory, a burner was designed and built at the University of Gothenburg (Sweden) to generate submicron soot particles with adjustable, albeit interdependent particle size distributions, BC fractions, and mixing states with organics. This soot generator differs from the widely used miniature combustion aerosols standard (mini-CAST, Jing, Ltd., Zollikofen, Switzerland), which generates soot in an N<sub>2</sub>-quenched, laminar diffusion flame [31]. Our soot generator uses a combination of premixing and diffusion of air in propane-fueled, air-quenched flame to provide maximum operating range (OC mass fraction range of 0–0.95) to produce BC- or OC-rich aerosol and improve the applicability/versatility of the soot generator design. Different flame conditions were realized by changing the flow rate of each gas line and, therefore, the Fuel–Air Equivalence Ratios ( $\Phi$ ).

### 2.2. Experimental Setup

A schematic flowchart of the experimental setup is shown in Figure 1. The aerosol from the combustion chamber was dried in a silica gel diffusion dryer prior to further analysis or modification. The dried aerosol was size selected for the study of monodisperse particles using a differential mobility analyzer (DMA1, model 3081, TSI Inc., Shoreview, MN, USA, aerosol flow rate 0.4 L min<sup>−1</sup>, and sheath flow rate 3.0 L min<sup>−1</sup>) located behind a bipolar charger (<sup>63</sup>Ni). For selected studies on the poly-disperse aerosol, DMA1 was bypassed. A thermo-denuder (TD) was used to remove the primary organic coating from the surface of soot particles [32]. The TD was maintained at 400 °C with a residence time of ~20 s. At this temperature, a constant average loss rate of 17% is observed for the size range of 50–400 nm, as shown in Figure S1 in the Supplementary Information. This loss rate was applied for the correction of the loss of number concentration, e.g., by diffusion and thermophoresis. Therefore, a measure of the fresh soot, i.e., a mixture of pure BC and OC, was obtained when no thermo-denuder (NTD) was used. The TD temperature was set up at 400 °C from the perspective that organic coatings present on the BC surfaces were negligible [33,34]. While one of the studies, Gkatzelis et al. (2016) [35], reported a fraction of POA does not evaporate completely from biomass burning and car engine exhaust due to low-volatile POA during combustion. It is also noteworthy that propane flame has a constant volume fraction after varying temperatures from 300 °C up to 500 °C, and no significant tar balls were formed at 400 °C.

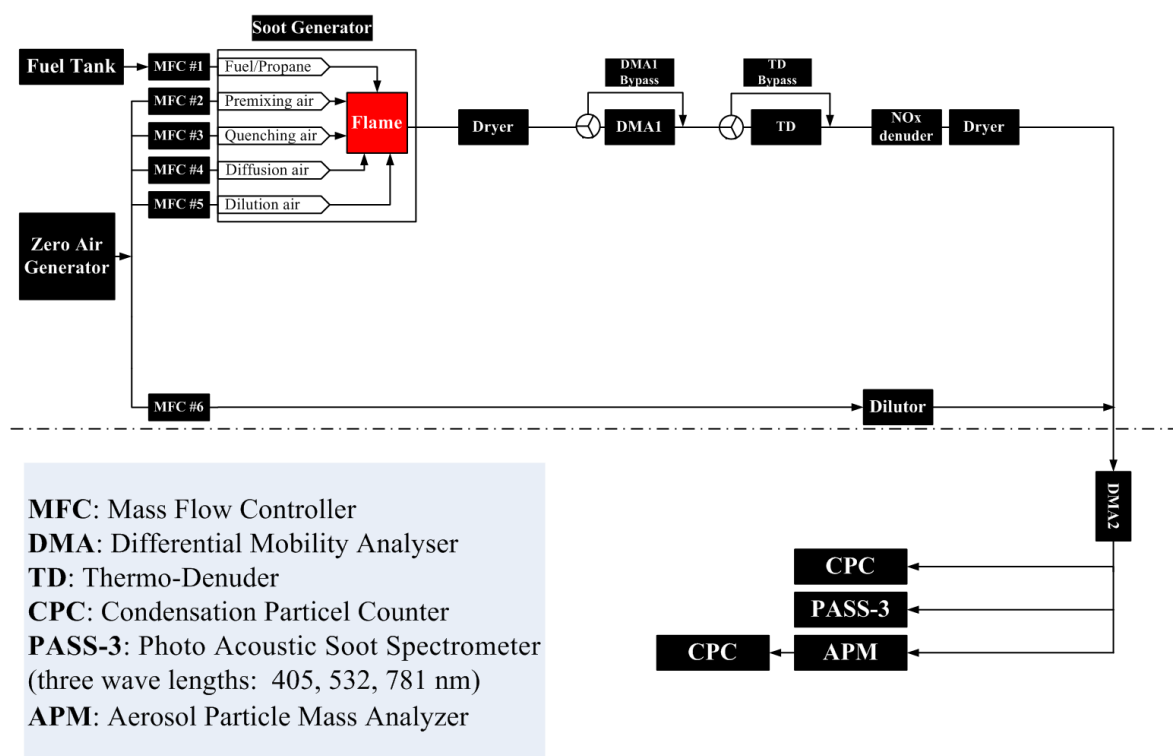


**Figure 1.** Schematic of flame characterization experimental setup.

Measurements on pure BC particles were performed when the aerosol was passed through TD. After the TD, charcoal granules (Activated Charcoal Powder USP, Spectrum Chemical Mfg. Corp., Gardena, CA, 90248) were used in the NO<sub>x</sub> denuder to remove NO<sub>x</sub>. A volatility tandem DMA (VTDMA) system was used to determine the mixing state of the soot aerosol [36]. This system consists of the two DMAs, i.e., DMA1 and DMA2, a condensation particle counter (CPC, model 3775, TSI Inc., Shoreview, MN, USA, flow rate 0.3 L min<sup>-1</sup>), and a TD arranged as shown in Figure 1. The OC and BC mass fraction was determined using the VTDMA system and an aerosol particle mass analyzer (APM, model APM-3600, Kanomax FMT, Inc., St Paul, MN 55110, United States). The light absorption coefficient of soot particle under the TD and TND conditions were measured by a photoacoustic soot spectrometer (PASS-3, Droplet Measurement Technologies Inc., Longmont, CO, USA) at three wavelengths, i.e., 405 nm, 532 nm, and 781 nm. The major components of the setup and infrastructure are described below.

### 2.3. Instruments

#### 2.3.1. Size Distribution with DMA + CPC

A DMA (DMA2) (Vienna type, length 280 mm, inner/outer radius 25.0/33.3 mm, aerosol flow rate 1.6 L min<sup>-1</sup>, and sheath flow rate 10.0 L min<sup>-1</sup>) and a CPC shown in Figure 1 were used to measure the number size distributions (9–430 nm) of both fresh soot particles and thermo-denuded samples. Thermo-denuded samples refer to the BC particles, which were classified into size bins based on their mobility diameter,  $D_p$ . The DMA2 + CPC system was used in two modes. In the first mode, the system was used as a scanning mobility particle sizer (SMPS) that measured the soot particle size distributions. These distributions were then used to determine the mode of the soot mobility diameter of the complete size distribution. In the second mode, the system was used as part of the VTDMA system that monitored changes in the particle mobility diameter. This mode was also used to select the mobility diameter for the subsequent APM and PASS-3 measurements.

### 2.3.2. Particle Mass Mobility Relationship Using a DMA-APM System

The particle mass mobility relationship and, hence, the effective density were determined using the DMA2, an APM, and a CPC in series followed by previous literature McMurry et al. (2002) [37] and shown in Figure 1. After selecting a given mobility diameter of particles using the DMA2, the median mass representing individual particles of the population was determined. The APM consisted of two concentric cylinders rotating at the same angular speed. A voltage was applied over the cylinders and the particles introduced in the gap between these cylinders experienced a centrifugal force. Particles with a specific mass-to-charge ratio where the electric force equals the centrifugal force were transmitted by the APM and counted with the CPC [38]. The DMA-APM-CPC system was calibrated using polystyrene latex spheres (Duke Scientific Corp., USA), following the previously described methodology [37]. In addition, the mass sensitivity of multiply charged particles was determined, and the overestimation of the mass was found to be negligible for all soot-particle sizes considered.

### 2.3.3. Absorption Measurements with PASS-3

A PASS-3 was used to simultaneously measure the in situ light absorption coefficients of particles at wavelengths of 405, 532, and 781 nm, with a time resolution of 2 s [39] and at a sampling flow of 0.8 L min<sup>-1</sup>. The laser beam power was square-wave modulated at the acoustic resonance frequency of the resonator. Particles in the air-stream-absorbed light, leading to periodic heating of the gas in the resonator. An acoustic pressure wave was created through absorption-induced gas expansion resulting from the heating. A microphone attached to one end of the resonator detected the acoustic signal, which was taken as the measure of light absorption. The piezo electrical disk located on the other end of the resonator was used to determine the acoustic resonance frequency of the resonator and the resonator quality factor (gain) for calibrating the system. The laser power was measured with the integrating sphere/photodetector. Strongly light-absorbing particles with a small amount of scattering generated from a kerosene lamp run in a fuel-rich mode were used to calibrate the absorption.

### 2.4. Flame Settings

Three flames were chosen (see Table 1 for corresponding settings). In all the experiments, the Fuel–Air Equivalence Ratio ( $\Phi$ ), i.e., the ratio of the fuel-to-oxidizer ratio and the stoichiometric fuel-to-oxidizer ratio, was calculated from the fuel flow rate and air flow rates, including the: premixing air, diffusion air, and dilution air. For comparison with the literature,  $C/O$  is estimated as  $C/O = 7.16 \times f_f/f_{air}$  [7], where  $f_f$  and  $f_{air}$  are flow rates of the propane fuel and the oxidation air (including the premixing air, diffusion air, and dilution air, but excluding the quenching, air), respectively. This exclusion was made assuming that the propane fuel is oxidized without input from the quenching air. For propane combustion under stoichiometric conditions,  $C/O$  is 0.30.

**Table 1.** Parameters of the three flame characterization experiments.

	Parameter	Exp. F1	Exp. F2	Exp. F3
# 1	Propane (mL min <sup>-1</sup> )	56	56	56
# 2	Premixing air (mL min <sup>-1</sup> )	82	57	57
# 3	Diffusion air (mL min <sup>-1</sup> )	1134	1134	888
# 4	Quenching air (mL min <sup>-1</sup> )	503	503	503
# 5	Dilution air (mL min <sup>-1</sup> )	0	0	0
	$C/O$	0.33	0.34	0.42
	$d/p$	13.8	19.9	15.6
	$\Phi^{\S}$ (Fuel–Air Equivalence Ratio)	1.10	1.12	1.41

# is the number mark for various parameters shown in Figure 1.  $d/p$  = diffusion-to-premixing air ratio;  $\Phi^{\S}$  (Fuel–Air Equivalence Ratio) = Fuel flow rate/(Flow rates of premixing air + diffusion air + dilution air)/(Stoichiometric ratio of C<sub>3</sub>H<sub>8</sub> to O<sub>2</sub> during complete combustion/Fraction of O<sub>2</sub> in air).

## 2.5. Data Analysis

### Morphology and Mixing State

The mass equivalent diameter  $D_{me}$  corresponds to a spherical particle of the same mass, and can be calculated from the particle mass  $m_p$  and the material density  $\rho_m$ :

$$D_{me} = \sqrt[3]{\frac{6m_p}{\pi\rho_m}}, \quad (1)$$

The flame exhaust particles contained BC and POA. The corresponding material density  $\rho_m$  can be calculated from:

$$\frac{m_{p,T}}{\rho_m} = \frac{m_{BC}}{\rho_{BC}} + \frac{m_{p,T} - m_{BC}}{\rho_{POA}}, \quad (2)$$

where  $m_{BC}$  and  $m_{p,T}$  are the BC mass (measured at T: 400 °C) and the total particle mass (measured at NTD: 25 °C), respectively.  $\rho_{BC}$  and  $\rho_{POA}$  are the material densities of BC (1.77 g cm<sup>-3</sup>) and POA (1.10 g cm<sup>-3</sup>).

The mass equivalent coating thickness  $\Delta r_{me}$  expressed as the difference in the particle  $D_{me}$  of the NTD and TD processes:

$$\Delta r_{me} = \frac{D_{me,NTD} - D_{me,TD}}{2}, \quad (3)$$

where  $D_{me,NTD}$  and  $D_{me,TD}$  are the mass equivalent diameters of the BC + POA particle and the BC core, respectively.

The particle diameter shrink factor,  $Sfd$  is calculated from:

$$Sfd = \frac{D_{p,NTD}}{D_{p,TD}}, \quad (4)$$

where  $D_{p,NTD}$  and  $D_{p,TD}$  are the mobility diameter of the BC + POA particle and the BC core, respectively.

The mass-mobility exponent,  $Dfm$  may be determined from:

$$m_p = K \cdot D_p^{Dfm}, \quad (5)$$

where  $D_p$  is the particle mobility diameter,  $m_p$  is the particle mass, and  $K$  is the experimentally determined scaling prefactor. The value of  $K$  depends on the overlap between the primary spherules in the aggregate and is related to the packing of the spherules in space.

The effective particle density  $\rho_{eff}$  can also be determined from simultaneous measurements of the mass and the mobility diameter and is calculated from:

$$\rho_{eff} = \frac{6m_p}{\pi D_p^3}, \quad (6)$$

The dynamic shape factor  $\chi$  of the particles can be calculated from the measured mobility diameter  $D_p$  and the volume equivalent diameter  $D_{ve}$ :

$$\chi = \frac{D_p C_{ve}}{D_{ve} C_p}, \quad (7)$$

where  $C_{ve}$  and  $C_p$  are the Cunningham slip correction factors for particles with diameters of  $D_{ve}$  and  $D_p$ , respectively. If we assume that the soot aggregates are free of internal void spaces, then  $D_{ve}$  is equal to the mass equivalent diameter  $D_{me}$ .

The void space fraction ( $F_{vs}$ ), i.e., volume of voids/total volume of particles determined from the mobility diameter, is calculated from the  $D_{me}$  and  $D_p$  of BC and BC + POA particles:

$$F_{vs} = 1 - \frac{D_{me}^3}{D_p^3}, \quad (8)$$

The relationship between the particle mass and the mobility diameter can be described by:

$$D_p = k' N_{pp}^x, \quad (9)$$

where  $k'$  and  $N_{pp}$  is the proportionality constant and the number of primary spherules (or monomers) in the soot aggregate, respectively.  $N_{pp}$  is proportional to the actual mass and  $x = 1/Dfm$ .

Several models have been proposed for describing the relationship between  $D_p$ ,  $N_{pp}$ , and the primary spherule diameter  $d_{pp}$  [40–42]. The model developed by Sorensen was used in this study (Equations (10) and (11)) [42], with one fixed exponent of  $N_{pp}$  to  $N_{pp} = 1000$  [38]. Calculations were performed assuming that the: (1) primary spherules of each aggregate were in point contact and (2) the material density of the primary spherules was the same as that ( $1.77 \text{ g cm}^{-3}$ ) of BC.

$$m_p = N_{pp} \cdot \frac{\pi}{6} \rho_{BC} d_{pp}^3, \quad (10)$$

$$D_p = d_{pp} N_{pp}^{0.46}, \quad N_{pp} < 1000, \quad (11)$$

The size-resolved mixing state of each flame was quantified. The mass concentration of internally mixed BC (int. BC), internally mixed POA (int. POA), and externally mixed POA (ext. POA) for each size at 25 °C are calculated from:

$$M_{int. BC} = m_{BC} \cdot N_{BC}, \quad (12)$$

$$M_{int. POA} = (m_{p,T} - m_{BC}) \cdot N_{BC}, \quad (13)$$

$$M_{ext. POA} = \frac{\pi}{6} \rho_{POA} D_p^3 \cdot (N_T - N_{BC}), \quad (14)$$

where  $N_{BC}$  and  $N_T$  are the BC number concentration (measured at TD: 400 °C) and the total particle number concentration (measured at NTD: 25 °C), respectively.  $D_p$  is the initial size of particles at 25 °C. Accordingly, the mass fraction of each component can be calculated from Equations (12)–(14). A framework for interpreting the state of the morphological transformation of soot exposed to heating was developed and illustrated in Figure 2 (see Section 3.3.2 for further details).

For wavelengths ranging from 405 nm to 781 nm, the AAE of particles is calculated as:

$$AAE = -\frac{\ln(b_{abs,781}) - \ln(b_{abs,405})}{\ln(781) - \ln(405)}, \quad (15)$$

where  $b_{abs,781}$  and  $b_{abs,405}$  are absorption coefficients at 781 and 405 nm, respectively, measured with PASS-3.

The mass absorption cross-section ( $MAC_{BC}$ ) refers to the capacity to absorb light per mass unit BC. The MAC of BC particles, i.e., the light absorbed/unit of mass concentration in air, is calculated from the absorption coefficient ( $b_{abs,BC}$ ), number concentration ( $N_{BC}$ ), and single particle mass ( $m_{BC}$ ) measured with DMA-APM and is given as follows:

$$MAC_{BC} = \frac{b_{abs,BC}}{m_{BC} \cdot N_{BC}}, \quad (16)$$

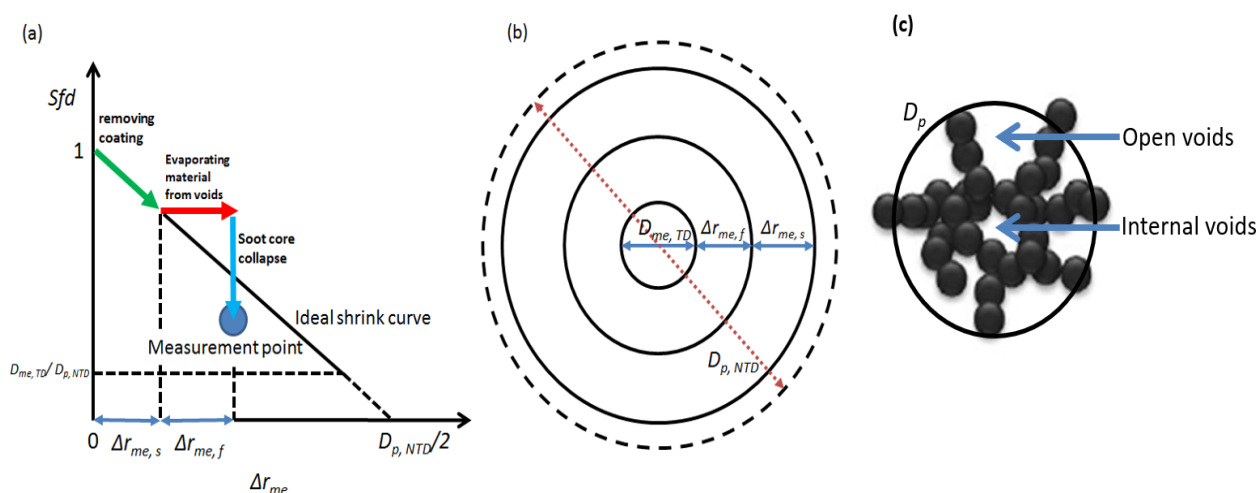


**Figure 2.** Framework for quantifying the state of the morphological transformation of soot exposed to heating. **(a)** particle diameter growth factor as a function of the coating thickness  $\Delta r_{me}$  associated with each measurement point. The ideal growth line, denoted by a black solid line, describes condensation of material on a perfect incompressible solid sphere with the same initial mobility diameter and mass as a fresh soot particle; **(b)** assumption of a concentric core shell structure; **(c)** soot undergoes stepwise morphological transformation, the fraction of internal voids and the fraction of open voids in the soot aggregation.

The MAC of light-absorbing organic particles ( $MAC_{Org}$ ) can be calculated from:

$$MAC_T = f_{BC}MAC_{BC} + f_{Org}MAC_{Org} = \frac{b_{abs,T}}{m_{p,T} \cdot N_T}, \quad (17)$$

where  $MAC_T$  and  $MAC_{Org}$  are the MAC values of the total light-absorbing particles and absorption from the organic mass fraction of particles, respectively.  $b_{abs,T}$ ,  $N_T$ , and  $m_{p,T}$  are the absorption coefficient, total number concentration, and single particle mass associated with the total number of light-absorbing particles, respectively.  $f_{BC}$  and  $f_{Org}$  are the respective mass fractions of BC and organic particles. The MAC values of both BC and organics for each flame were averaged over all particle sizes.

### 3. Results and Discussion

Measurement results of the absorption coefficient ( $b_{abs}$ ), particle mass ( $m_p$ ) as well as particle size obtained from TD and NTD setups were analyzed. The morphological and optical properties of BC and BrC were evaluated from the viewpoint of the mixing state determined from VTDMA measurements, differential absorption (i.e., AAE), and absorption potential (i.e., MAC derived from PASS-3).

#### 3.1. Composition of Soot

In this study, the soot particle was composed of two main components: BC and POA. The C/O ratios for Exp. F1, Exp. F2 and Exp. F3, i.e., 0.33, 0.34, and 0.42, respectively, were all higher than the C/O (0.30) for a stoichiometric reaction. This indicated that all three flames were fuel-rich. Figure 3a–c shows the average value of the size-resolved mass of BC and POA representing a single particle and the POA mass fraction. The mass fraction was determined by comparing the APM-measured mass of the particles before and after heating with adjusted thermal losses in the thermo-denuder and, as the figure shows, this fraction contributed 20% to 40% of the total particle mass (BC + POA). For the flames in Exp. F1 and Exp. F3, the mechanism of POA formation was size-dependent, i.e., the POA fraction decreased with increasing  $D_p$ . In contrast, a relatively constant fraction of ~21% was obtained for the flame in Exp. F2. The POA formation mechanism and the size

dependence of the POA fraction may be influenced by the diffusion-to-premixing air (i.e.,  $d/p$ ) ratio. For example, the size dependence of the POA mass fraction changed from strong to negligible when the  $d/p$  ratio increased from 13.8 to 19.9 (see the red arrows in Figures 3 and S2 in the Supplementary Information). This suggests that a decrease in the  $d/p$  ratio had possibly enhanced the formation of POA fraction on the smaller size BC particle surfaces. Almost the same POA fraction (i.e., ~20%) was obtained for the largest size bin (250 nm) associated with all three flames, suggesting that the regulation of premixing or diffusion air had a negligible impact on this size bin.

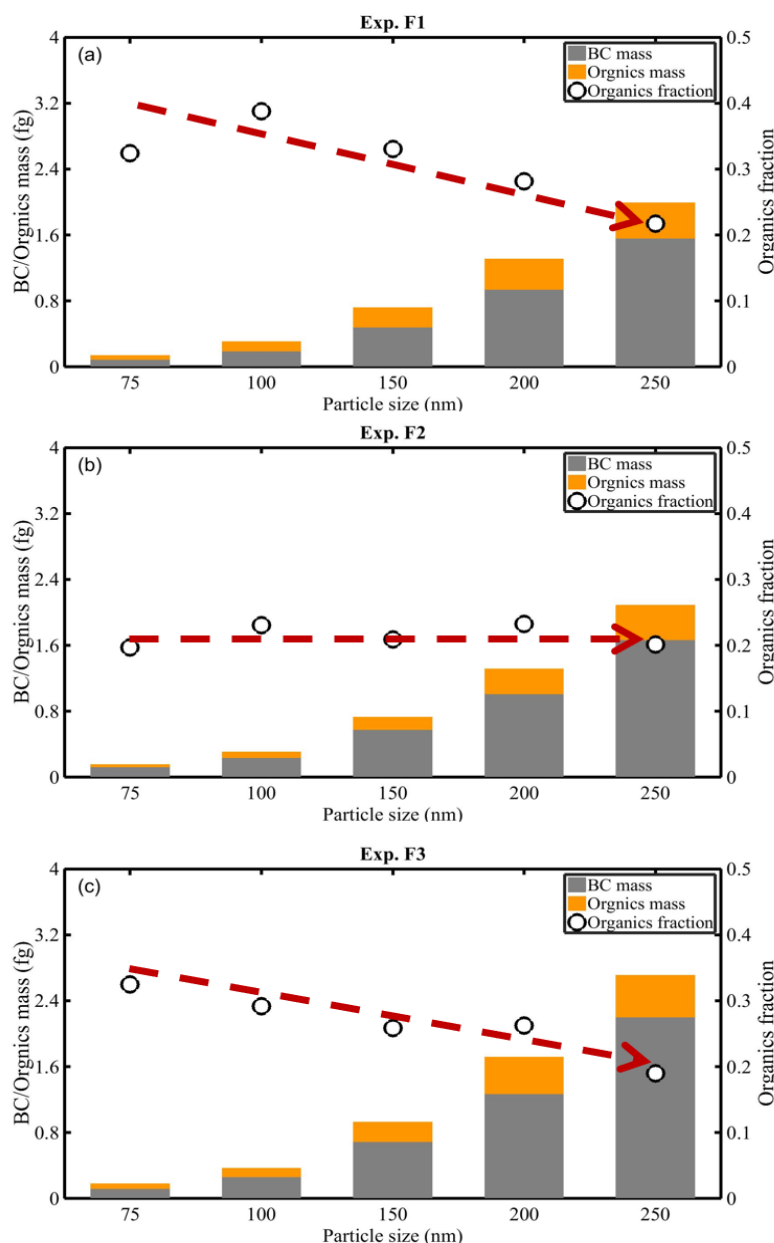


**Figure 3.** (a–c): Mass of BC and POA in a single particle, and POA fraction for various sizes of particles associated with flames of Exp. F1, Exp. F2 and Exp. F3 at 25 °C (BC + POA) and 400 °C (pure BC). Note:  $p/d$  ratios of 13.8, 19.9, and 15.6 are obtained for Exp. F1, Exp. F2 and Exp. F3, respectively.

### 3.2. Constitution of the BC Particles

The size-resolved masses of pure BC and BC + POA mixture particles were measured, and morphological parameters were determined for the 75, 100, 150, 200 and 250 nm particles from all three flames. Table 2 shows the fitted values of the scaling prefactor ( $K$ )

and the mass mobility exponent ( $Dfm$ ;  $Dfm = 3$  for a population of spherical particles) for the size-resolved particles of each flame at 25 °C and 400 °C.  $Dfm$  values ranged from 2.13 to 2.34, consistent with the literature [43,44]. Parameters such as the diameter of a primary spherule (a building block of any soot aggregate) and the number of primary spherules in a soot aggregate ( $d_{pp}$  and  $N_{pp}$ , respectively, shown in Table 3) were determined via the Sorensen model [42]. These findings are consistent with those of previous studies [38].  $N_{pp}$  in the BC aggregates increased with increasing  $d_p$ , whereas  $d_{pp}$  was essentially constant for the entire  $D_p$  range of each flame in Exp. F1, Exp. F2 and Exp. F3. These results indicated that BC aggregates in all three flames were formed through diffusion-limited cluster-cluster aggregation (DLCA) of primary spherules [42]. Similar  $d_{pp}$  values were obtained for each size in Exp. F1 and Exp. F2. However, the  $N_{pp}$  values in Exp. F2 were (in general) larger than those in Exp. F1, owing to the smaller  $D_p$  of BC aggregates in Exp. F1 at 400 °C. In contrast,  $d_{pp}$  values in Exp. F3 were, in general, larger than those in both Exp. F1 and Exp. F2, indicating that a decrease in the premixing air did not affect the  $d_{pp}$ , but a decrease in the diffusion air resulted in the formation of relatively large size primary spherules. The primary spherule diameter obtained in this study (~20–29 nm) was comparable to those of diesel soot [38] and Mini-CAST soot obtained under fuel-lean conditions [45]. Therefore, scientific investigations in this study are very relevant to the atmosphere. This study also highlights the significance of emissions, formation, and mixing of black and brown carbon in the combustion processes, as discussed in the following sections.

**Table 2.** Scaling prefactor ( $K$ ) and mass–mobility exponent ( $Dfm$ ) of different flame particles at different temperatures.

Flame Condition	$K (\times 10^{-5})$	$Dfm$
Exp. F1, 25 °C	0.96	2.25
Exp. F1, 400 °C	0.97	2.23
Exp. F2, 25 °C	1.4	2.18
Exp. F2, 400 °C	1.5	2.13
Exp. F3, 25 °C	1.1	2.27
Exp. F3, 400 °C	0.65	2.34

**Table 3.** Model results of  $d_{pp}$  and  $N_{pp}$  for different sizes of flame particles at 400 °C.

Initial $D_p$ (nm) and Conditions	$D_p$ (nm)	$d_{pp}$ (nm)	$N_{pp}$
Exp. F1, 75 nm, modeled	63	21.4	10
Exp. F1, 100 nm, modeled	84	23.0	17
Exp. F1, 150 nm, modeled	129	23.0	42
Exp. F1, 200 nm, modeled	180	21.7	100
Exp. F1, 250 nm, modeled	225	22.2	153
Exp. F2, 75 nm, modeled	72	21.3	14
Exp. F2, 100 nm, modeled	93	23.1	21
Exp. F2, 150 nm, modeled	145	21.2	65
Exp. F2, 200 nm, modeled	193	19.7	143
Exp. F2, 250 nm, modeled	242	19.9	229
Exp. F3, 75 nm, modeled	70	22.6	12
Exp. F3, 100 nm, modeled	93	26.3	16
Exp. F3, 150 nm, modeled	146	25.9	43
Exp. F3, 200 nm, modeled	186	28.6	58
Exp. F3, 250 nm, modeled	242	27.8	111

### 3.3. Mixing State

#### 3.3.1. Size Distribution and Size-Resolved Mixing State

The mixing state of BC and POA was determined by measuring the flame exhaust with TD (400 °C) and NTD (25 °C) setups integrating VTDMA. Figure 4a–c shows the

poly-disperse aerosol particle number size distributions of pure BC and the BC + POA mixture considered in Exp. F1, Exp. F2 and Exp. F3, respectively.

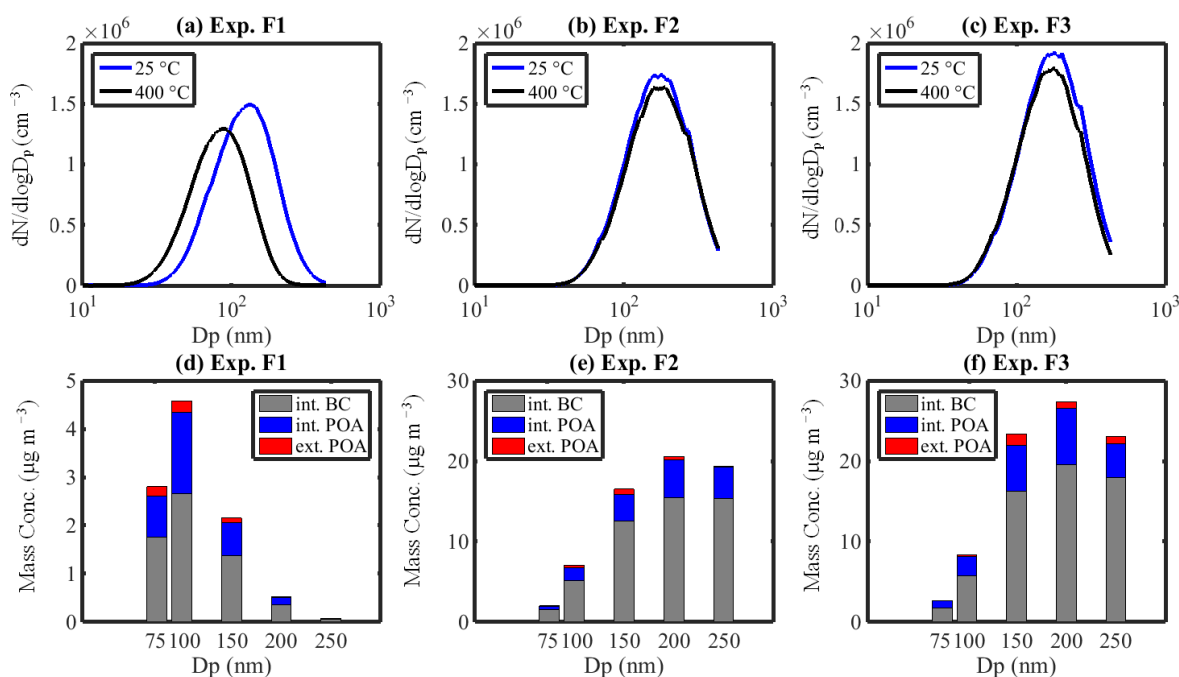


**Figure 4.** Number size distributions of particles in flames of (a) Exp. F1, (b) Exp. F2 and (c) Exp. F3 at 25 °C and 400 °C. Mass concentration and mixing state of the size-resolved soot from (d) Exp. F1, (e) Exp. F2 and (f) Exp. F3 at 25 °C, the components are plotted additively.

The poly-dispersed soot aerosol from the flame in Exp. F1 was log-normally distributed (Figure 4a) with a mode peak at 130 nm corresponding to the total number concentration of particles ( $7.8 \times 10^5 \text{ cm}^{-3}$ ) at 25 °C. When the same soot aerosol was heated to 400 °C, the mode peak size and the total particle number concentration decreased significantly to 90 nm and  $6.4 \times 10^5 \text{ cm}^{-3}$ , respectively. This suggested that the soot was composed of externally (~18% of the particles, by number, which evaporated completely) as well as internally mixed (~82%, which shrank from an initial size of 130 nm to 90 nm) BC and POA. Table 4 shows the size-resolved (i.e., 75, 100, 150, 200, and 250 nm) mono-disperse particle number fraction of internally mixed BC/POA and externally mixed POA, measured with VTDMA. The table also shows the mass fraction of each component of all three flames. The mass fraction results reveal that 7% of the 75 nm particles were externally mixed, whereas only 2% of the 250 nm particles were externally mixed, indicating that externally mixed POA was mainly formed in a size range smaller than 75 nm, which is consistent with the previous studies [46,47]. In fact, externally mixed POA was formed by homogeneous nucleation of organic vapors followed by their condensational growth from the same vapors and/or through condensation of these organic vapors on the nanoparticles of organic carbon (NOC). Small (size: 1–10 nm) primary organic carbon was formed in hydrocarbon combustion reactions [47], and externally mixed POA was formed by condensational growth and coagulation of these small size NOC. The formations of internally mixed and externally mixed POA competed with each other in the process of condensational growth. Since the surface area of preexisting BC particles was obviously larger than externally mixed POA particles, the concentrations of externally mixed POA remained limited, and externally mixed POA particles could not grow too large sizes further; the coagulation of externally mixed POA particles with BC particle's surface had also suppressed its own formation.

**Table 4.** Mobility diameter ( $D_p$ ), mass equivalent diameter ( $D_{me}$ ), void space fraction ( $F_{vs}$ ), coating thickness ( $\Delta r_{me}$ ), diameter shrink factor ( $Sfd$ ), and number/mass fraction of each component for 75, 100, 150, 200 and 250 nm particles from Exp. F1, Exp. F2 and Exp. F3.

Exp. No.	$D_{p,NTD}$ (nm)	$D_{p,TD}$ (nm)	$m_{p,NTD}$ (fg)	$m_{p,TD}$ (fg)	$D_{me,NTD}$ (nm)	$D_{me,TD}$ (nm)	$F_{vs,NTD}$ (%)	$F_{vs,TD}$ (%)	$\Delta r_{me}$ of Coated Particle (nm)	$Sfd$	Number Fraction (%)		Mass Fraction (%)		
											Internally Mixed BC/POA	Externally Mixed POA	Internally Mixed BC	Internally Mixed POA	Externally Mixed POA
F1	75	63	0.14	0.09	55.9	46.8	59	57	4.6	0.84	96	4	63	30	7
	100	84	0.31	0.19	73.2	58.8	61	63	7.2	0.84	97	3	58	37	5
	150	129	0.72	0.48	96.3	80.3	74	74	8.0	0.86	98	2	64	31	5
	200	180	1.31	0.94	117.0	100.5	80	79	8.3	0.90	99	1	70	28	2
	250	225	1.99	1.56	133.4	118.9	85	84	7.2	0.90	99	1	76	21	3
F2	75	72	0.16	0.13	57.0	51.5	56	62	2.8	0.96	99	1	79	19	2
	100	93	0.31	0.24	71.6	63.4	63	66	4.1	0.93	97	3	73	22	5
	150	145	0.73	0.58	95.4	85.4	74	78	5.0	0.97	99	1	76	20	4
	200	193	1.32	1.01	116.4	102.9	80	84	6.7	0.96	99	1	75	23	2
	250	242	2.09	1.67	135.1	121.6	84	86	6.8	0.97	100	0	80	20	0
F3	75	70	0.19	0.12	61.3	51.3	45	59	5.0	0.93	99	1	67	32	1
	100	93	0.37	0.26	76.9	65.7	54	62	5.6	0.93	98	2	69	28	3
	150	146	0.93	0.69	104.1	90.7	67	73	6.7	0.97	97	3	70	24	6
	200	186	1.72	1.27	127.9	111.1	74	77	8.4	0.93	99	1	72	25	3
	250	242	2.71	2.20	147.2	133.3	80	81	6.9	0.97	99	1	77	18	5

The flame in Exp. F2 was produced by reducing the flow rate of the premixing air from  $82 \text{ mL min}^{-1}$  to  $57 \text{ mL min}^{-1}$  while employing the same flame parameters as those used in Exp. F1. Consequently, the flame of Exp. F2 yielded distinctly different soot, i.e., exhibiting a larger peak mode ( $\sim 175 \text{ nm}$ ) from that produced by Exp. F1. The poly-dispersed aerosol from the flame in Exp. F2 was also log-normally distributed (Figure 4b) with a total number concentration of particles of  $9.4 \times 10^5 \text{ cm}^{-3}$  at  $25^\circ\text{C}$  and  $9.1 \times 10^5 \text{ cm}^{-3}$  at  $400^\circ\text{C}$ . Peak modes at  $175 \text{ nm}$  occurred (without shrinkage) at both temperatures. A BC number fraction of 97% suggested that the flame in Exp. F2 consisted mainly of internally mixed particles and only a small amount (3%) of externally mixed POA. These results indicated that the particle size distribution and the mixing state could be significantly changed by reducing the amount of premixing air (i.e., increasing the fuel-to-premixing-air ( $f/p$ ) ratio). The monodisperse aerosol determined the size-resolved mixing state of the particles, as shown in Table 4. For example, number fraction of 1%, 3%, 1%, 1% and 0% of the 75, 100, 150, 200 and 250 nm particles were externally mixed, respectively. In addition, the  $D_p$  of particles in the flame of Exp. F2 decreased less than the  $D_p$  of particles in Exp. F1 (Table 4). This indicates a significant collapse of the soot core in Exp. F2 was prevented owing to the smaller mass fraction of internally mixed POA compared with that occurring in Exp. F1. At small POA fractions, the surface tension force exerted by the condensed POA was lower than that required for the collapse of the soot aggregate during heating.

The flame of Exp. F3 evolved from the flame of Exp. F2 when the diffusion air flow rate was reduced from  $1134 \text{ mL min}^{-1}$  (Exp. F2) to  $888 \text{ mL min}^{-1}$  (Exp. F3). The poly-dispersed aerosol in the flame of Exp. F3 was also log-normally distributed (Figure 4c) with a total number concentration of particles of  $1.03 \times 10^6 \text{ cm}^{-3}$  at  $25^\circ\text{C}$  and  $9.6 \times 10^5 \text{ cm}^{-3}$  at  $400^\circ\text{C}$ . As in Exp. 2, the peak modes of the flame in Exp. F3 occurred at  $175 \text{ nm}$  for both temperatures. Unlike the reduction in the premixing air flow rate, the reduction in the diffusion air flow rate did not influence the number size distributions of particles. The number distributions, although characterized by higher concentrations, were like those obtained for Exp. F2 (Figure 4b,c). In general, the mass fraction of each component of the mono-disperse soot from Exp. F3 was identical to that of the soot from Exp. F2, shown in Table 4.

### 3.3.2. Morphological Transformation

When BC- and POA-containing particles were heated to  $400^\circ\text{C}$ , changes in the morphological structure of the soot were probably influenced mainly by the evaporation of POA. In our previous study, we used the pure BC derived from Exp. F1 to investigate the morphological transformation of soot via condensation of SOA and sulfuric acid. We also developed a framework for quantifying the fraction of open voids in the soot aggregate [48]. Extending this framework to the evaporation of POA from internally mixed BC, another framework was developed for quantifying the state of the morphological transformation of soot. This transformation describes the utilization of material for shrinkage stemming from the removal of the condensed material from the BC particle surface and voids, as shown in Figure 2. Figure 2a shows the particle diameter shrink factor ( $Sfd$ ) as a function of the reduction in mass equivalent coating thickness ( $\Delta r_{me}$ ) associated with each measurement point. The ideal shrink curve, denoted by a solid black line, describes the removal of condensed material from a perfect incompressible solid sphere with the same initial mass equivalent diameter as a pure BC particle.

Three processes are outlined in the framework, namely, (i) removal of the POA layer coated onto the BC surface. This removal was characterized by a decrease in the mobility diameter as a function of  $\Delta r_{me}$  along or parallel to the ideal shrink curve, (ii) removal of POA that filled the open voids of the BC aggregate. This removal was characterized by a constant  $Sfd$  as a function of  $\Delta r_{me}$  parallel to the  $x$ -axis and (iii) a decrease in the mobility diameter due to the collapse of the BC core. Here, the collapse of the BC core is defined as the decrease in mobility diameter by rearrangement of primary spherule, but not due to evaporation of material mass. During this collapse, primary spherules of soot were rearranged, owing to

the surface forces exerted by evaporating POA. The shrinkage process was characterized by the decrease in  $Sfd$  as a function of  $\Delta r_{me}$  parallel to the  $y$ -axis. Processes (i)–(iii) are denoted by solid green, red and blue lines, respectively, in Figure 2a. Our previous study Pei et al. (2018) [48] showed that preferential filling of the open voids was followed by surface growth and sequential filling of internal voids upon the condensation of additional material, i.e., SOA. Using these insights and extending this framework to model the evaporation process, we propose that the evaporated material should first be completely accommodated by the open voids and then form extra material on the surface coatings. We postulate that after the combustion, the BC- and organics-containing material leaving off the flame undergoes a transformation. During this transformation, the process of internal voids filled by organics is largely restricted by the time scale (less than a fraction of a second) for condensation [49]. The time available is insufficient for vapors to reach the internal voids, leading to vapor deposition mainly on open voids.

The pathway to the actual measurement points represented a combination of one or more of the three aforementioned processes. Figure 5 shows the  $Sfd$  as a function of  $\Delta r_{me}$  for the 75, 100, 150, 200, and 250 nm particles from Exp. F1, Exp. F2 and Exp. F3. Figure 5 also shows one possible pathway if the volume of open voids was larger than the volume of internally mixed POA; the particle underwent processes (ii) and (iii), denoted by the red and cyan color lines, respectively. If the measurement point is above the ideal shrink curve, then some fraction of the evaporated material must have been in the voids and preferentially in the open voids. If all the evaporated material was in the voids, the collapse was inevitable. If the measurement point is on the ideal shrink curve, then the possibilities of all three pathways arise. All the evaporated material perhaps was partially/entirely in the voids or partially on the surface. If the entire evaporated material was in the voids, the collapse of the BC core was equivalent to the volume of material evaporated from voids. In the case that the shrink point was below the ideal shrink curve, then the partial collapse of the BC core was inevitable. It should be noted that entire evaporated material can never be accommodated for the surface growth because the surface of the void is a subset of the void volume. This framework provides insights to dissect the mixing state and morphological transformation of soot. In order to better use this framework, measurements at different temperatures should be performed to obtain the in-situ states of the morphology and mixing state of the soot particle.

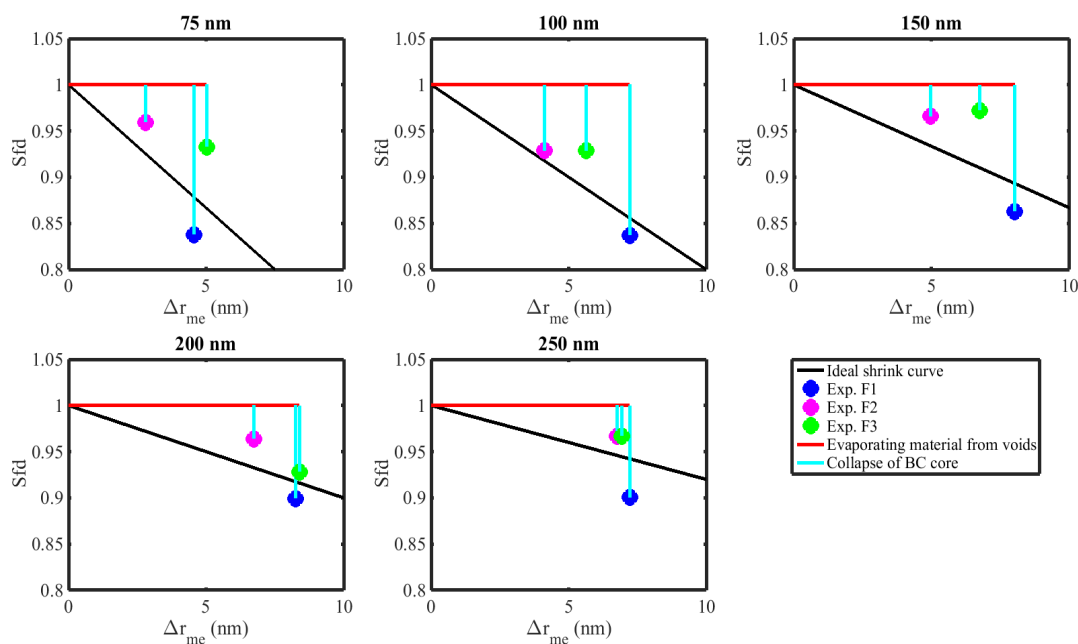


**Figure 5.** Diameter shrink factor ( $Sfd$ ) as a function of the coating thickness ( $\Delta r_{me}$ ) of 75, 100, 150, 200, and 250 nm particles from Exp. F1, Exp. F2 and Exp. F3.

### 3.4. Effective Density

Figure 6 shows the effective density ( $\rho_{eff}$ ) of pure BC and the BC + POA mixture (i.e., particles at 400 °C and 25 °C, respectively) from the three flames as a function of the particle mobility diameter ( $D_p$ ). In general,  $\rho_{eff}$  decreased with increasing  $D_p$  in all cases, consistent with previous observations that the morphology of both pure BC and BC + POA particles became increasingly irregular with increasing particle size. This was directly attributable to the fractal-like structure of the BC aggregates. However, the  $\rho_{eff}$  values of pure BC differed slightly from those of the BC + POA particles in the respective size bins. These differences, i.e.,  $\rho_{eff,BC} < \rho_{eff,BC+POA}$  were attributed primarily to the removal of internally mixed POA from particles heated to 400 °C. Except for the flame in Exp. F1 where  $\rho_{eff,BC} = \rho_{eff,BC+POA}$ , the heating had a negligible effect on  $D_p$ . This resulted probably from the fact that the BC core associated with the flame in Exp. F1 collapsed relatively more upon heating, thereby offsetting the effects of material removal. The decrease in  $\rho_{eff}$  in this study is consistent with those of Moore et al. (2014) [45], who reported that the  $\rho_{eff}$  of the soot particle from a fuel-rich flame of Mini-CAST decreased upon heating.

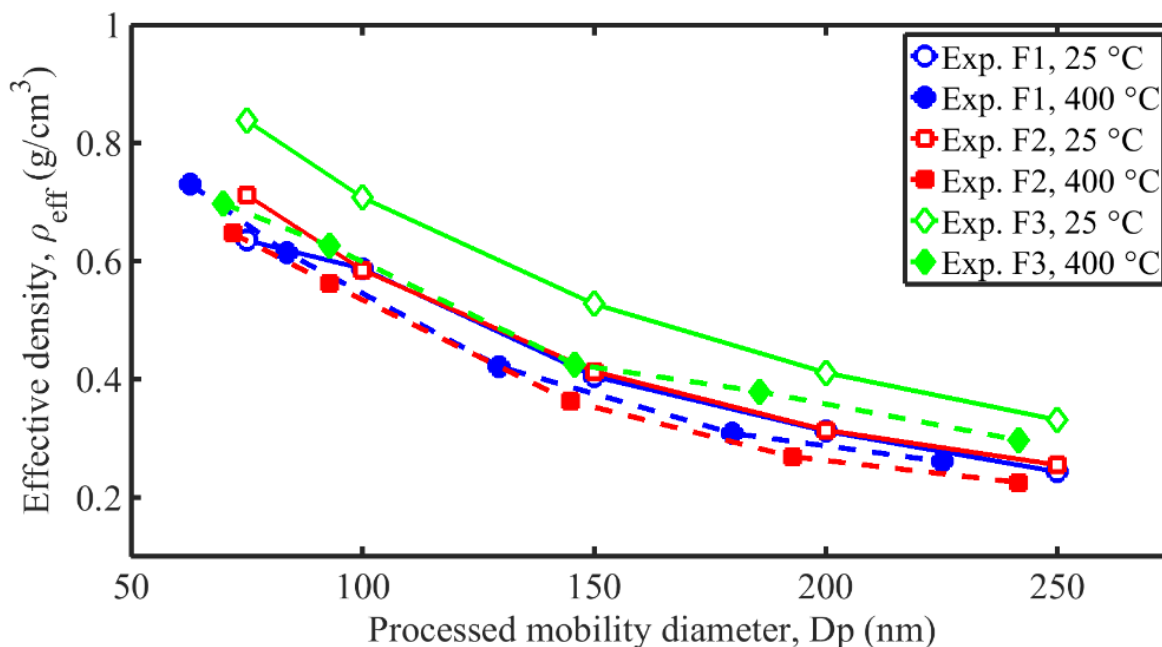


**Figure 6.** Effective density of particles in the flame characterization experiments after the TD hold at 25 °C (open symbols) and 400 °C (closed symbols).

### 3.5. Dynamic Shape Factor

If the fraction of internal voids ( $F_i$ ) and the fraction of open voids ( $F_o$ ) (where  $F_i = 1 - F_o$ ) in the soot aggregate are known, then the volume equivalent diameter, including internal voids ( $D_{ve,i}$ ), is given as:

$$D_{ve,i} = \sqrt[3]{D_{me}^3 + D_p^3 F_{vs} F_i} \quad (18)$$

This equation is derived using the concept of conservation of volume when materials are added. The dynamic shape factor, inclusive of internal voids, can then be derived from Equation (7). Figure 7 shows the dynamic shape factor ( $\chi$ ) of particles from Exp. F1 as a function of  $D_p$  without internal voids at 25 °C/400 °C and with internal voids at 400 °C. The fraction of internal voids ( $F_i$ ) is estimated to be 0.90, 0.91, 0.91, and 0.83 for 75, 100, 150, and 200 nm BC particles, respectively [48], and a fraction of 0.83 is also assumed for 250 nm BC particles. If internal voids are accounted for,  $D_{ve}$  was larger than  $D_{me}$ , and the resulting  $\chi$  was smaller than that obtained when these voids were neglected [50]. Generally,  $\chi$  increased with increasing  $D_p$  of the BC + POA mixture at 25 °C.  $\chi$  of BC at 400 °C without

internal voids increased with increasing  $D_p$ , but  $\chi$  of BC at 400 °C with internal voids became significantly smaller (1.04–1.08). This indicated that the consideration of internal voids yielded almost spherical BC particles, which resulted from the collapse induced by the removal of condensed material in voids upon heating. These results indicate that internal voids occupy considerable space and the traditional method of calculating  $\chi$  is not representative of the prediction of in situ sphericity of BC particles.

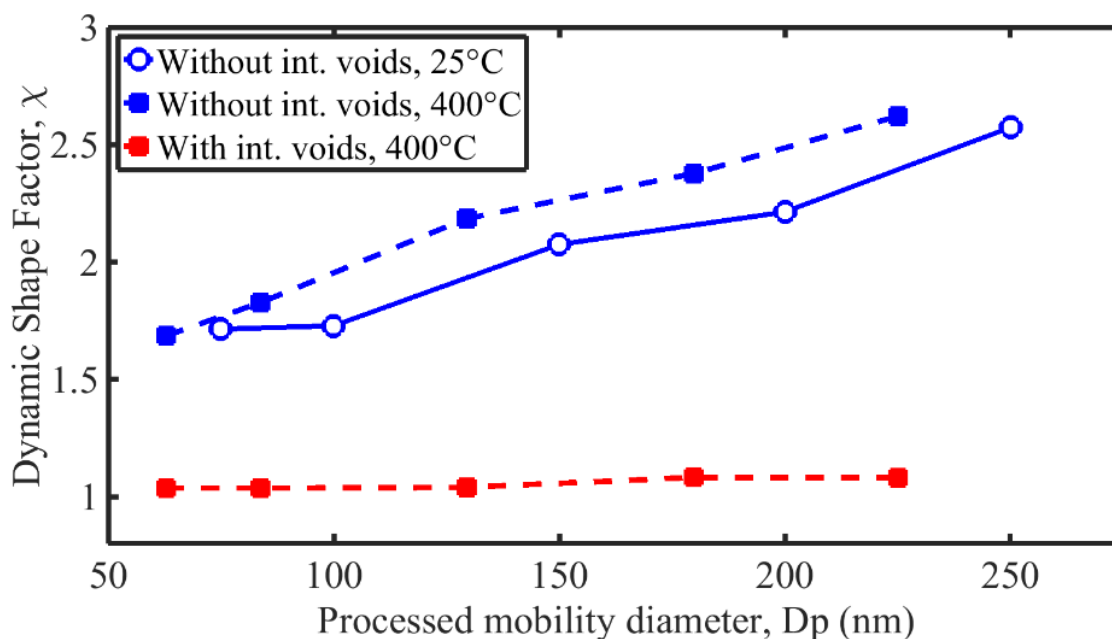


**Figure 7.** Dynamic shape factor of particles from Exp. F1 without internal voids at 25 °C/400 °C and with internal voids at 400 °C.

### 3.6. Optical Properties

#### 3.6.1. Size-Resolved Differential Light Absorption of BC and POA at Various Wavelengths

The AAE parameter is used to describe the differential absorption of light at different wavelengths for various sizes of particles. Figure 8a–c shows the AAE of particles in the flames of Exp. F1, Exp. F2 and Exp. F3 at 25 °C (BC + POA) and 400 °C (pure BC). Average  $AAE_{405/781}$  values of  $2.06 \pm 0.11$ ,  $1.65 \pm 0.08$ , and  $1.84 \pm 0.06$  corresponding to BC + POA mixture and average values of  $1.01 \pm 0.12$ ,  $1.08 \pm 0.11$  and  $1.28 \pm 0.07$  associated with pure BC are obtained for Exp. F1, Exp. F2 and Exp. F3, respectively. These values are arithmetic averages across the various sizes, and the uncertainties were calculated from the error propagation law, and those are shown in Figure 8 as the error bars. At the lower concentrations of particles, the uncertainty became larger. The wavelengths of 405 nm and 781 nm were chosen to better separate BrC and BC since BrC can absorb light at both 405 nm and 532 nm, but the absorption at 781 nm was negligible. The  $AAE_{405/781}$  values indicated that, at all sizes, the three flames contained a significant amount of light-absorbing BrC. The average size-resolved values are like the theoretical value of AAE for pure BC (i.e., 1), indicating that strongly light absorbing POA (i.e., BrC) was co-produced in all three flames.

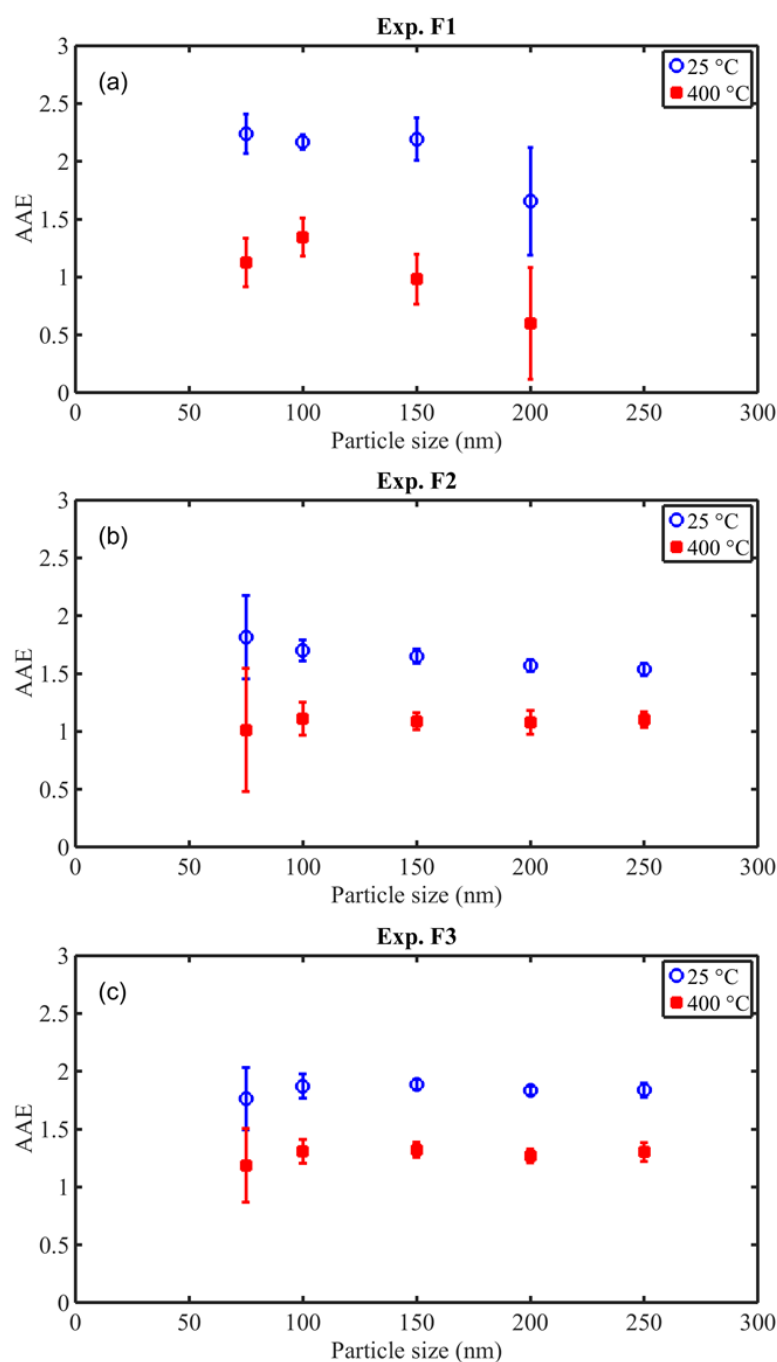


**Figure 8.** (a–c): Ångström Absorption Exponent (AAE) for various sizes of particles in the flames associated with Exp. F1, Exp. F2 and Exp. F3 at 25 °C (BC + POA) and 400 °C (pure BC). AAE is calculated from 405 nm and 781 nm absorption data.

### 3.6.2. MAC of BC and POA

Figure 9a–c shows MAC values of BC and POA for each flame at three wavelengths. These values are arithmetic averages across various sizes, and the uncertainties were calculated from the variation of signals in instruments based on the error propagation law. The MAC value of  $7.5 \text{ m}^2 \text{ g}^{-1}$  for BC recommended by Bond and Bergstrom (2006) [4] was used to calculate the theoretical values of MAC at each wavelength with the assumption that the theoretical AAE for BC was 1.0. It revealed that the MACs for BC were higher than those of POA at both long and short wavelengths. This is consistent with a previous study [1], where light-absorbing organics seemed to absorb more light at shorter wavelengths than at

longer wavelengths. Comparable MACs were obtained for the BC of all three flames for each size, suggesting that in our flames, the absorptive nature of pure BC did not depend on the combustion conditions, and BC from different flames had a similar molecular structure. However, for each wavelength, the measured MAC values of each flame were all lower than the theoretical value (presented in dashed line), indicating that the BC particles from the flames in this study had more  $sp^3$ -bonded carbon than  $sp^2$ -bonded carbon in the molecules since  $sp^3$ -bonded carbon does not absorb light, while the  $sp^2$ -bonded carbon absorbs light strongly.

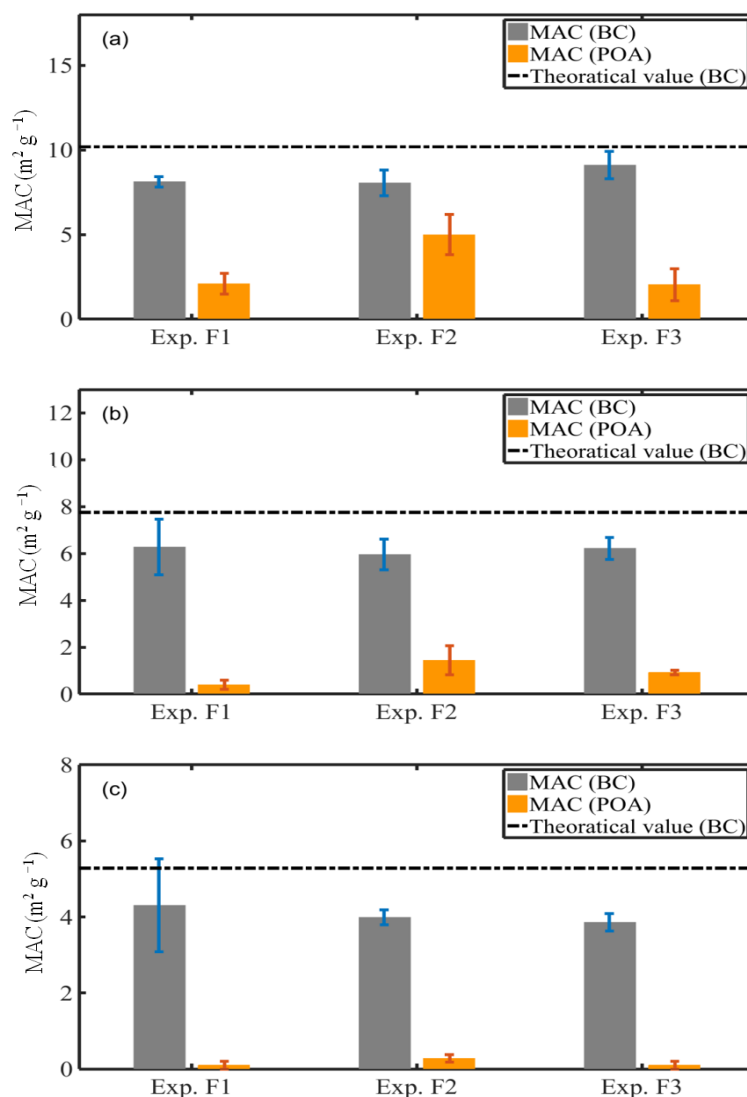


**Figure 9.** Mass absorption cross-section (MAC) for particles in flames of Exp. F1, Exp. F2, and Exp. F3 at wavelengths of (a) 405 nm, (b) 532 nm, and (c) 781 nm. The dashed lines show the theoretical values of pure BC. The deviations can be attributed to the ratio of  $sp^2$  to  $sp^3$  hybridized carbon atoms.

### 3.6.3. Contribution of BrC to Absorption

We compare the MAC values and the imaginary RI values of POA ( $k_{POA}$ ) obtained from the measurements in this study. The MAC values of POA in all three flames were estimated at wavelengths 405, 532, and 781 nm. Figure 10 shows the MAC of POA from this study compared with literature values for POA formed via propane combustion as described in Lu et al. (2015) [27] and Kim et al. (2015) [51] and extracted from biomass samples [5]. The MAC and the corresponding imaginary RI of POA ( $k_{POA}$ ) are plotted as

a function of the wavelength. The  $k_{POA}$  values obtained in this study are calculated from Sun et al. (2007) [52]:

$$k_{POA} = \frac{\rho_{POA}\lambda}{4\pi\zeta} MAC_{POA}, \quad (19)$$

where  $\lambda$  is the wavelength and  $\rho_{POA}$  is the material density of the POA (assumed to be  $1.10 \text{ g cm}^{-3}$ ).  $\zeta$  is only weakly dependent on  $k_{POA}$ , representing the particulate effect compared to the bulk solution. For organics where the real part of RI is  $n = 1.5$ , and the particles are smaller than the wavelength of light used,  $\zeta$  ranges from 0.69 to 0.75 [52]. In this study, the average value of  $\zeta$  (i.e., 0.72) is used to determine  $k_{POA}$ .

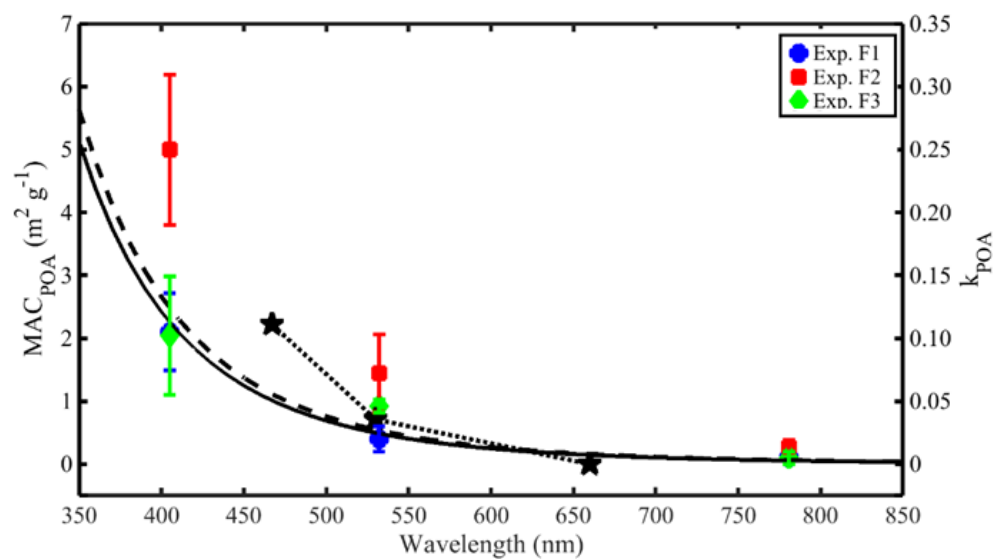


**Figure 10.** MAC and estimated imaginary refractive index of POA ( $k_{POA}$ ) as a function of the wavelength ( $\lambda$ ). The black stars denote  $k_{POA}$  (from Kim et al. (2015) [51]) of particles associated with propane combustion. The black dotted line denotes  $k_{POA}$  and the corresponding MAC estimated from a polynomial fit (equation:  $k_{POA} = 1.4304 - 6.49 \times 10^{-3}\lambda + 1.0126 \times 10^{-5}\lambda^2 - 5.3939 \times 10^{-9}\lambda^3$ ) of  $k_{POA}$  obtained from Kirchstetter et al. (2004) [5]. The solid black line denotes  $k_{POA}$  and MAC calculated from  $k_{POA}$  for primary organic aerosol emitted from propane combustion at a carbon-to-oxygen atomic ratio (C/O) of 0.45 from Lu et al. (2015) [27]. The y-axis on the right side shows the corresponding  $k_{POA}$  for each MAC that was calculated from the formula proposed by Sun et al. (2007) [52].

At a short wavelength of 405 nm, the POA from all three flames exhibited strong absorption, which decreased significantly at longer wavelengths. As in the case of the MAC associated with propane combustion [27], the MAC of POA in all three flames was very small at 781 nm (see Figure 9), although the MAC of POA in Exp. 2 was still higher than those in Exp. F1 and Exp. F3. The measured MAC of POA at 405 nm from Exp. F1 was exceptionally high ( $MAC \ 5 \text{ m}^2 \text{ g}^{-1}$ ). The possible reason could be fuel-rich conditions during Exp. F1 and in the absence of low-oxygen, propane combustion can potentially produce the tarball (a type POA), which possibly resembled the properties of the BC. At 405 nm, the POA in Exp. F1 and Exp. F3 had the same MAC, whereas the POA in Exp. F2 had a much higher MAC. At 532 nm, the flames in Exp. F2 and Exp. F3 had comparable MACs of  $\sim 1.5 \text{ m}^2 \text{ g}^{-1}$  and  $\sim 1 \text{ m}^2 \text{ g}^{-1}$ , respectively, while the flame in Exp. F1 had a MAC of almost zero. Compared to the generalized parameterization, which is relevant to the atmosphere proposed by Lu et al. (2015) [27], POA in Exp. F1 and Exp. F3 was similar to the parameterization. However, POA in Exp. F2 exhibited a stronger light absorptive nature than what was previously reported; this, however, was similar to that reported by [51] (black stars in Figure 10), at least at shorter wavelengths. The discrepancies indicate the low level of scientific understanding of BrC formation and properties. It further suggests that flame conditions possibly had a significant influence on the MAC of organics which

we hypothesize to depend on the molecular composition of the POA particle. The flame setting in Exp. F2 corresponded to the highest diffusion-to-premixing air ( $d/p$ ) ratio. This setting possibly resulted in co-produced POA with stronger light-absorption ability at all wavelengths than the ability of the POA in Exp. F1 and Exp. F3. Caution should be taken when comparing experiments from various studies as the POA may differ among studies, thereby resulting in different  $k_{POA}$  values, depending on the method used. However, in all the experiments compared, the MAC and  $k_{POA}$  decreased with increasing wavelength. Furthermore, at wavelengths larger than 530 nm, the POAs all exhibited weak absorption with MAC values of  $<1.5 \text{ m}^2 \text{ g}^{-1}$ , whereas the MAC of BC at 530 nm was  $\sim 6 \text{ m}^2 \text{ g}^{-1}$  in this study. The differences in the  $k_{POA}$  values at wavelengths shorter than 530 nm may have resulted from differences in the molecular composition of POA originating from different emission sources. Absorption of POA is thought to increase almost continuously with an increasing degree of conjugation of the aromatic rings [53]. This indicated that the particles from the flame of Exp. F2 had the largest amount of polycyclic aromatic hydrocarbon (PAH) or PAH-like materials, owing possibly to the high  $d/p$  ratio setting of this flame.

#### 4. Conclusions

The particle mass–mobility relationship was measured with a DMA-APM system, and a framework for quantifying the in situ morphological properties of BC mixed with POA was developed. The in situ dynamic shape factor, which is significantly lower than that obtained using the traditional method, which neglects the internal voids in the soot aggregate, was derived from the new framework. The light absorption coefficient was measured with PASS-3, while MAC of both BC and POA, AAE of both the BC + POA mixture and pure BC, and the contribution of BrC to the total absorption was quantified.

The mass–mobility measurements were interpreted by using the new framework to derive the morphological transformation. This transformation consisted of processes where (i) the evaporation of externally mixed POA and the evaporation of internally mixed POA led to a decrease in the number concentration and the size of monodisperse aerosol, respectively; (ii) externally mixed BC was absent, as evidenced by a single peak of reduced size; (iii) collapse of the BC core was induced by the evaporation of POA from voids upon heating. In general, for all three flames, POA was internally mixed with BC of all sizes. Perhaps the POA in situ filled in the open voids in the soot aggregates. The key limitation of this study is that it focused on a model fuel propane combustion, which is different from biomass burning and diesel and gasoline fuel combustion. Therefore, the POA produced from propane can differ from biomass burning POA and diesel/gasoline POA.

The AAE at 405/781 nm of BC + POA was usually higher than 1.5 in all sizes for all three flames, indicative of the highly absorptive nature of POA. Extremely high MAC values of POA ( $2\text{--}5 \text{ m}^2 \text{ g}^{-1}$ ) were measured at 405 nm. This strong light-absorbing BrC, believed to be co-produced with BC, was attributed to the incomplete combustion of fuel. The flame settings, i.e., premixing and diffusion air flows, have a significant influence on the MAC values of POA. We hypothesize that these values depend on the molecular composition of the BrC, where a larger MAC indicates a higher degree of conjugation of aromatic rings in the composition compared with smaller values.

**Supplementary Materials:** The following supporting information can be downloaded at: <https://www.mdpi.com/article/10.3390/atmos13081270/s1>, Figure S1: Particle loss rates at 25 °C and 400 °C in the thermo-denuder (TD) as a function of particle size; Figure S2: POA mass fraction as a function of the  $d/p$  ratio associated with Exp. F1, Exp. F2 and Exp. F3. POA mass fraction was averaged from five sizes soot shown in Figure 3.

**Author Contributions:** Conceptualization, R.K.P.; Data curation, J.P., K.M. and H.R.M.; Formal analysis, K.M. and H.R.M.; Methodology, X.P. and R.K.P.; Investigation, J.P. and R.K.P.; Software, E.L. and X.P.; Resources, R.K.P.; Supervision, R.K.P.; Validation, X.P. and J.P.; Visualization, X.P.; Writing—original draft, J.P. and X.P.; Writing—review and editing, J.P., X.P., E.L. and R.K.P. All authors have read and agreed to the published version of the manuscript.

**Funding:** This research supported by Swedish Research Council for Environment, Agricultural Sciences and Spatial Planning (FORMAS: Project No. 214-2011-1183), and The APC was fully waived off to Jai Prakash with discount voucher code [966505694d9c399e].

**Institutional Review Board Statement:** Not applicable.

**Informed Consent Statement:** Not applicable.

**Data Availability Statement:** The data presented in this study are available on request from the corresponding author-Ravi Kant Pathak: ravikant@chem.gu.se.

**Acknowledgments:** The authors are sincerely grateful to Swedish Research Council for Environment, Agricultural Sciences and Spatial Planning Modelling the Regional and Global Earth system (MERGE) and Climate, Biodiversity and Ecosystem services (ClimBEco) for the financial support. The authors also acknowledge the technical and experimental support provided by our group members.

**Conflicts of Interest:** The authors declare no conflict of interest.

## References

1. Bond, T.C.; Doherty, S.J.; Fahey, D.W.; Forster, P.M.; Berntsen, T.; Deangelo, B.J.; Flanner, M.G.; Ghan, S.; Kärcher, B.; Koch, D.; et al. Bounding the role of black carbon in the climate system: A scientific assessment. *J. Geophys. Res. Atmos.* **2013**, *118*, 5380–5552. [[CrossRef](#)]
2. UNEP; WMO. *Integrated Assessment of Black Carbon and Tropospheric Ozone*; Publishing Services Section at the United Nations Office at Nairobi (UNON): Nairobi, Kenya, 2011.
3. IPCC. *Climate Change 2021: The Physical Science Basis. Working Group I Contribution to the IPCC Sixth Assessment Report*; IPCC: Geneva, Switzerland, 2021; p. 3949. [[CrossRef](#)]
4. Bond, T.C.; Bergstrom, R.W. Light Absorption by Carbonaceous Particles: An Investigative Review. *Aerosol Sci. Technol.* **2006**, *40*, 27–67. [[CrossRef](#)]
5. Kirchstetter, T.W.; Novakov, T.; Hobbs, P.V. Evidence that the spectral dependence of light absorption by aerosols is affected by organic carbon. *J. Geophys. Res. D Atmos.* **2004**, *109*, 1–12. [[CrossRef](#)]
6. Laskin, A.; Laskin, J.; Nizkorodov, S.A. Chemistry of Atmospheric Brown Carbon. *Chem. Rev.* **2015**, *115*, 4335–4382. [[CrossRef](#)]
7. Schnaiter, M.; Gimmler, M.; Llamas, I.; Linke, C.; Jäger, C.; Mutschke, H. Strong spectral dependence of light absorption by organic carbon particles formed by propane combustion. *Atmos. Chem. Phys.* **2006**, *6*, 2981–2990. [[CrossRef](#)]
8. China, S.; Mazzoleni, C.; Gorkowski, K.; Aiken, A.C.; Dubey, M.K. Morphology and mixing state of individual freshly emitted wildfire carbonaceous particles. *Nat. Commun.* **2013**, *4*, 2122. [[CrossRef](#)]
9. Stephens, M.; Turner, N.; Sandberg, J. Particle identification by laser-induced incandescence in a solid-state laser cavity. *Appl. Opt.* **2003**, *42*, 3726. [[CrossRef](#)]
10. Lee, A.K.Y.; Willis, M.D.; Healy, R.M.; Onasch, T.B.; Abbatt, J.P.D. Mixing state of carbonaceous aerosol in an urban environment: Single particle characterization using the soot particle aerosol mass spectrometer (SP-AMS). *Atmos. Chem. Phys.* **2015**, *15*, 1823–1841. [[CrossRef](#)]
11. Onasch, T.B.; Trimborn, A.; Fortner, E.C.; Jayne, J.T.; Kok, G.L.; Williams, L.R.; Davidovits, P.; Worsnop, D.R. Soot particle aerosol mass spectrometer: Development, validation, and initial application. *Aerosol Sci. Technol.* **2012**, *46*, 804–817. [[CrossRef](#)]
12. Khalizov, A.F.; Hogan, B.; Qiu, C.; Petersen, E.L.; Zhang, R. Characterization of soot aerosol produced from combustion of propane in a shock tube. *Aerosol Sci. Technol.* **2012**, *46*, 925–936. [[CrossRef](#)]
13. Ghazi, R.; Tjong, H.; Soewono, A.; Rogak, S.N.; Olfert, J.S. Mass, mobility, volatility, and morphology of soot particles generated by a mckenna and inverted burner. *Aerosol Sci. Technol.* **2013**, *47*, 395–405. [[CrossRef](#)]
14. Graves, B.; Olfert, J.; Patychuk, B.; Dastanpour, R.; Rogak, S. Characterization of Particulate Matter Morphology and Volatility from a Compression-Ignition Natural-Gas Direct-Injection Engine. *Aerosol Sci. Technol.* **2015**, *49*, 589–598. [[CrossRef](#)]
15. Momenimovahed, A.; Olfert, J.S. Effective Density and Volatility of Particles Emitted from Gasoline Direct Injection Vehicles and Implications for Particle Mass Measurement. *Aerosol Sci. Technol.* **2015**, *49*, 1051–1062. [[CrossRef](#)]
16. Sakurai, H.; Park, K.; McMurry, P.H.; Zarling, D.D.; Kittelson, D.B.; Ziemann, P.J. Size-Dependent Mixing Characteristics of Volatile and Nonvolatile Components in Diesel Exhaust Aerosols. *Environ. Sci. Technol.* **2003**, *37*, 5487–5495. [[CrossRef](#)] [[PubMed](#)]
17. Lin, P.; Aiona, P.K.; Li, Y.; Shiraiwa, M.; Laskin, J.; Nizkorodov, S.A.; Laskin, A. Molecular Characterization of Brown Carbon in Biomass Burning Aerosol Particles. *Environ. Sci. Technol.* **2016**, *50*, 11815–11824. [[CrossRef](#)] [[PubMed](#)]
18. Liu, C.; Chung, C.E.; Zhang, F.; Yin, Y. The colors of biomass burning aerosols in the atmosphere. *Sci. Rep.* **2016**, *6*, 28267. [[CrossRef](#)]
19. Saleh, R.; Robinson, E.S.; Tkacik, D.S.; Ahern, A.T.; Liu, S.; Aiken, A.C.; Sullivan, R.C.; Presto, A.A.; Dubey, M.K.; Yokelson, R.J.; et al. Brownness of organics in aerosols from biomass burning linked to their black carbon content. *Nat. Geosci.* **2014**, *7*, 647–650. [[CrossRef](#)]

20. Liu, J.; Bergin, M.; Guo, H.; King, L.; Kotra, N.; Edgerton, E.; Weber, R.J. Size-resolved measurements of brown carbon in water and methanol extracts and estimates of their contribution to ambient fine-particle light absorption. *Atmos. Chem. Phys.* **2013**, *13*, 12389–12404. [[CrossRef](#)]
21. Olson, M.R.; Garcia, M.V.; Robinson, M.A.; Van Rooy, P.; Diitenberger, M.A.; Bergin, M.; Schauer, J.J. Investigation of black and brown carbon multiple-wavelength- dependent light absorption from biomass and fossil fuel combustion source emissions. *J. Geophys. Res. Atmos.* **2015**, 6682–6697. [[CrossRef](#)]
22. Chakrabarty, R.K.; Moosmüller, H.; Chen, L.W.A.; Lewis, K.; Arnott, W.P.; Mazzoleni, C.; Dubey, M.K.; Wold, C.E.; Hao, W.M.; Kreidenweis, S.M. Brown carbon in tar balls from smoldering biomass combustion. *Atmos. Chem. Phys.* **2010**, *10*, 6363–6370. [[CrossRef](#)]
23. Graber, E.R.; Rudich, Y. Atmospheric HULIS: How humic-like are they? A comprehensive and critical review. *Atmos. Chem. Phys.* **2006**, *6*, 729–753. [[CrossRef](#)]
24. Laskin, J.; Laskin, A.; Nizkorodov, S.A.; Roach, P.; Eckert, P.; Gilles, M.K.; Wang, B.; Lee, H.J.; Hu, Q. Molecular selectivity of brown carbon chromophores. *Environ. Sci. Technol.* **2014**, *48*, 12047–12055. [[CrossRef](#)] [[PubMed](#)]
25. Schnaiter, M.; Horvath, H.; Möhler, O.; Naumann, K.H.; Saathoff, H.; Schöck, O.W. UV-VIS-NIR spectral optical properties of soot and soot-containing aerosols. *J. Aerosol Sci.* **2003**, *34*, 1421–1444. [[CrossRef](#)]
26. Moise, T.; Flores, J.M.; Rudich, Y. Optical Properties of Secondary Organic Aerosols and Their Changes by Chemical Processes. *Chem. Rev.* **2015**, *115*, 4400–4439. [[CrossRef](#)]
27. Lu, Z.; Streets, D.G.; Winijkul, E.; Yan, F.; Chen, Y.; Bond, T.C.; Feng, Y.; Dubey, M.K.; Liu, S.; Pinto, J.P.; et al. Light Absorption Properties and Radiative Effects of Primary Organic Aerosol Emissions. *Environ. Sci. Technol.* **2015**, *49*, 4868–4877. [[CrossRef](#)] [[PubMed](#)]
28. Feng, Y.; Ramanathan, V.; Kotamarthi, V.R. Brown carbon: A significant atmospheric absorber of solar radiation. *Atmos. Chem. Phys.* **2013**, *13*, 8607–8621. [[CrossRef](#)]
29. Liu, J.; Scheuer, E.; Dibb, J.; Ziemba, L.D.; Thornhill, K.L.; Anderson, B.E.; Wisthaler, A.; Mikoviny, T.; Devi, J.J.; Bergin, M.; et al. Brown carbon in the continental troposphere. *Geophys. Res. Lett.* **2014**, *41*, 2191–2195. [[CrossRef](#)]
30. Park, R.J.; Kim, M.J.; Jeong, J.I.; Youn, D.; Kim, S. A contribution of brown carbon aerosol to the aerosol light absorption and its radiative forcing in East Asia. *Atmos. Environ.* **2010**, *44*, 1414–1421. [[CrossRef](#)]
31. Jing, L. Standard Combustion Aerosol Generator (SCAG) for Calibration Purposes. *Atmos. Environ.* **1999**, *27*, 1271–1275.
32. Huffman, J.A.; Ziemann, P.J.; Jayne, J.T.; Worsnop, D.R.; Jimenez, J.L. Development and characterization of a fast-stepping/scanning thermodeuder for chemically-resolved aerosol volatility measurements. *Aerosol Sci. Technol.* **2008**, *42*, 395–407. [[CrossRef](#)]
33. Takhar, M.; Stroud, C.A.; Chan, A.W.H. Volatility Distribution and Evaporation Rates of Organic Aerosol from Cooking Oils and their Evolution upon Heterogeneous Oxidation. *ACS Earth Space Chem.* **2019**, *3*, 1717–1728. [[CrossRef](#)]
34. Kolesar, K.R.; Li, Z.; Wilson, K.R.; Cappa, C.D. Heating-Induced Evaporation of Nine Different Secondary Organic Aerosol Types. *Environ. Sci. Technol.* **2015**, *49*, 12242–12252. [[CrossRef](#)]
35. Gkatzelis, G.I.; Papanastasiou, D.K.; Florou, K.; Kaltsonoudis, C.; Louvaris, E.; Pandis, S.N. Measurement of nonvolatile particle number size distribution. *Atmos. Meas. Tech.* **2016**, *9*, 103–114. [[CrossRef](#)]
36. Burtscher, H.; Baltensperger, U.; Bukowiecki, N.; Cohn, P.; Hüglin, C.; Mohr, M.; Matter, U.; Nyeki, S.; Schmatloch, V.; Streit, N.; et al. Separation of volatile and non-volatile aerosol fractions by thermodesorption: Instrumental development and applications. *J. Aerosol Sci.* **2001**, *32*, 427–442. [[CrossRef](#)]
37. McMurry, P.H.; Wang, X.; Park, K.; Ehara, K. The relationship between mass and mobility for atmospheric particles: A new technique for measuring particle density. *Aerosol Sci. Technol.* **2002**, *36*, 227–238. [[CrossRef](#)]
38. Rissler, J.; Messing, M.E.; Malik, A.I.; Nilsson, P.T.; Nordin, E.Z.; Bohgard, M.; Sanati, M.; Pagels, J.H. Effective density characterization of soot agglomerates from various sources and comparison to aggregation theory. *Aerosol Sci. Technol.* **2013**, *47*, 792–805. [[CrossRef](#)]
39. Arnott, W.P.; Moosmüller, H.; Rogers, C.F.; Jin, T.; Bruch, R. Photoacoustic spectrometer for measuring light absorption by aerosol: Instrument description. *Atmos. Environ.* **1999**, *33*, 2845–2852. [[CrossRef](#)]
40. Lall, A.A.; Rong, W.; Mädler, L.; Friedlander, S.K. Nanoparticle aggregate volume determination by electrical mobility analysis: Test of idealized aggregate theory using aerosol particle mass analyzer measurements. *J. Aerosol Sci.* **2008**, *39*, 403–417. [[CrossRef](#)]
41. Schmidt-Ott, A.; Baltensperger, U.; Gäggeler, H.W.; Jost, D.T. Scaling behaviour of physical parameters describing agglomerates. *J. Aerosol Sci.* **1990**, *21*, 711–717. [[CrossRef](#)]
42. Sorensen, C.M. The mobility of fractal aggregates: A review. *Aerosol Sci. Technol.* **2011**, *45*, 765–779. [[CrossRef](#)]
43. Pagels, J.; Khalizov, A.F.; McMurry, P.H.; Zhang, R.Y. Processing of soot by controlled sulphuric acid and water condensation mass and mobility relationship. *Aerosol Sci. Technol.* **2009**, *43*, 629–640. [[CrossRef](#)]
44. Park, K.; Cao, F.; Kittelson, D.B.; McMurry, P.H. Relationship between particle mass and mobility for diesel exhaust particles. *Environ. Sci. Technol.* **2003**, *37*, 577–583. [[CrossRef](#)]
45. Moore, R.H.; Ziemba, L.D.; Dutcher, D.; Beyersdorf, A.J.; Chan, K.; Crumeyrolle, S.; Raymond, T.M.; Thornhill, K.L.; Winstead, E.L.; Anderson, B.E. Mapping the operation of the miniature combustion aerosol standard (Mini-CAST) soot generator. *Aerosol Sci. Technol.* **2014**, *48*, 467–479. [[CrossRef](#)]
46. Maricq, M.M. Examining the relationship between black carbon and soot in flames and engine exhaust. *Aerosol Sci. Technol.* **2014**, *48*, 620–629. [[CrossRef](#)]

47. Sgro, L.A.; Borghese, A.; Speranza, L.; Barone, A.C.; Minutolo, P.; Bruno, A.; D'Anna, A.; D'Alessio, A. Measurements of nanoparticles of organic carbon and soot in flames and vehicle exhausts. *Environ. Sci. Technol.* **2008**, *42*, 859–863. [[CrossRef](#)]
48. Pei, X.; Hallquist, M.; Eriksson, A.C.; Pagels, J.; Donahue, N.M.; Mentel, T.; Svenningsson, B.; Brune, W.; Pathak, R.K. Morphological transformation of soot: Investigation of microphysical processes during the condensation of sulfuric acid and limonene ozonolysis product vapors. *Atmos. Chem. Phys.* **2018**, *18*, 9845–9860. [[CrossRef](#)]
49. Violi, A.; Voth, G.A.; Sarofim, A.F. A time-scale problem for the formation of soot precursors in premixed flames. *ACS Div. Fuel Chem. Prepr.* **2003**, *48*, 545–547.
50. DeCarlo, P.F.; Slowik, J.G.; Worsnop, D.R.; Davidovits, P.; Jimenez, J.L. Particle morphology and density characterization by combined mobility and aerodynamic diameter measurements. Part 1: Theory. *Aerosol Sci. Technol.* **2004**, *38*, 1185–1205. [[CrossRef](#)]
51. Kim, J.; Bauer, H.; Dobovičnik, T.; Hitztenberger, R.; Lottin, D.; Ferry, D.; Petzold, A. Assessing optical properties and refractive index of combustion aerosol particles through combined experimental and modeling studies. *Aerosol Sci. Technol.* **2015**, *49*, 340–350. [[CrossRef](#)]
52. Sun, H.; Biedermann, L.; Bond, T.C. Color of brown carbon: A model for ultraviolet and visible light absorption by organic carbon aerosol. *Geophys. Res. Lett.* **2007**, *34*, 1–5. [[CrossRef](#)]
53. Andreae, M.O.; Gelencsér, A. Black carbon or brown carbon? the nature of light-absorbing carbonaceous aerosols. *Atmos. Chem. Phys.* **2006**, *6*, 3131–3148. [[CrossRef](#)]